Quantum-orbit analysis of high-order-harmonic generation by resonant plasmon field enhancement

T. Shaaran,[1] M. F. Ciappina,[1] and M. Lewenstein[1,2]
[1]*ICFO-Institut de Ciències Fotòniques, E-08860 Castelldefels, Barcelona, Spain*
[2]*ICREA-Institució Catalana de Recerca i Estudis Avançats, Lluis Companys, E-08010 Barcelona, Spain*
(Received 25 June 2012; published 10 August 2012)

We perform a detailed analysis of high-order harmonic generation (HHG) in atoms within the strong field approximation (SFA) by considering spatially inhomogeneous monochromatic laser fields. We investigate how the individual pairs of quantum orbits contribute to the harmonic spectra. We show that in the case of inhomogeneous fields the electron tunnels with two different canonical momenta. One of these momenta leads to a higher cutoff and the other one develops a lower cutoff. Furthermore, we demonstrate that the quantum orbits have a very different behavior in comparison to the homogeneous field. We also conclude that in the case of the inhomogeneous fields both odd and even harmonics are present in the HHG spectra. Within our model, we show that the HHG cutoff extends far beyond the standard semiclassical cutoff in spatially homogeneous fields. Our findings are in good agreement both with quantum-mechanical and classical models.

DOI: 10.1103/PhysRevA.86.023408 PACS number(s): 32.80.Rm, 42.65.Ky, 78.67.Bf

I. INTRODUCTION

In the context of the interaction of matter with strong laser fields, the high-order harmonics generation (HHG) process [1,2] has attracted considerable interest since it represents a viable route to the generation of coherent radiation in the ultraviolet (UV) to extreme ultraviolet (XUV) spectral range with high repetition rate. Due to this high repetition rate, as well as high coherence degree and wavelength tunability, HHG has found numerous applications in various areas of science, such as material sciences, life sciences, and lithography [3].

In addition, HHG has been employed for generating ultrashort pulses, and even single attosecond pulses [4]. This allows even more control over the atomic and molecular processes. For instance, by superposing the XUV pulses on the laser field, one can resolve dynamic processes in atoms or molecules with the precision of a few attoseconds [5]. The physics behind the HHG can be understood by a simple semiclassical three-step model [6]. According to this picture, an electron leaves the atom or molecule by tunneling through the potential barrier, formed by the atomic potential and the laser electric field, to reach the continuum. It subsequently propagates in the continuum and is driven back by the laser filed toward its parent ion or molecule. Finally, upon its return, it recombines with the core and leads to the emission of energetic photons.

The threshold intensity for generating high-order harmonic in noble gases is above 10^{13} W/cm^2, which is far beyond the output power of the current femtosecond oscillators. Nowadays, chirped-pulse amplification (CPA) is used to exceed the threshold intensity. CPA is a complex process and it requires multipass amplifier cavities in tandem. On the other hand, as far as the applications of the HHG are concerned, the optimization of HHG efficiency and the extension of the cutoff to the short-wavelength region are important aspects to consider [7,8]. The cutoff frequency of the generated harmonics can be extended either by reducing (increasing) the laser frequency (wavelength) or increasing the peak field amplitude. There are, however, limitations in tuning these parameters. In fact, reducing the laser frequency leads to a significant drop in the harmonic yield due to the longer electron excursion times [9,10], while increasing the laser field intensity produces depletion of the ground state.

A recent demonstration has shown that the surface plasmon resonance could provide a possible solution to overcome the problems cited above [11]. The local field enhancement induced by a resonant plasmon within a metallic nanostructure requires no extra cavities or laser pumping for amplification. In this scheme, the local electric fields can be intensified by more than 20 dB [12,13], an amplification that exceed the threshold laser intensity for HHG in noble gases. In addition, the pulse repetition rate remains unchanged without adding any additional cavities or extra pumping. Moreover, each nanostructure acts as a point-like source to generate harmonics radiation, which through constructive interference can provide even more focused coherent radiation. This gives a wide range of possibilities to spatially rearrange nanostructures to shape or enhance HHG spectral and even obtain a new physics. The locally enhanced field has a distinct spatial dependency, which gives an enormous extension to the HHG cutoff [14].

HHG based on plasmonics can be understood as follows [11]: The external femtosecond low intensity pulse couples to the plasmon mode and induces a collective oscillation of free charges within the localized regions of the nanostructure. The free charges redistribute the electric field around the nanostructure vicinity, in such, to form a spot of highly enhanced electric field. The enhanced field, which largely depends on the geometrical shape of the metallic nanostructure, exceeds the threshold intensity required for HHG. As a result, by the injection of noble gases into the spot of the enhanced field, one can generate high-order harmonics. In Ref. [11], the output of the femtosecond oscillator, which was a pulse with 10-fs pulse duration, 800 nm of wavelength, and intensity of 10^{11} W/cm^2, was directly focused onto a bow-tie nanoantenna. As a result of the laser pulse interaction with the nanostructure, the field intensity is enhanced by two to four orders of magnitude, which is sufficient enough to produce XUV wavelengths from the seventh (114 nm) to the 21st (38 nm) harmonics in argon.

Hitherto, the theoretical approaches for studying strong field phenomena are largely based on the assumption that the laser electric field is spatially homogeneous in the region where

the electron motions take place [15,16]. This assumption, however, does not hold for the field enhanced by resonant plasmons. Indeed, the strong confinement of the electrons in the plasmonic hot spots generates a spatially inhomogeneous electric field, which strongly influences the subsequent motion of the electrons in the strong field phenomena. As a result, new physics will emerge in the interaction between matter and strong laser fields.

Since the first observation of HHG different theoretical models, including solving the time-dependent Schrödinger equation (TDSE) and the strong field approximation (SFA), have been applied to describe this phenomenon (for details see the review articles in Refs. [17,18]). On the other hand, the HHG by resonant plasmon field enhancement is a new topic and it has been considerably less well studied since it is far more difficult to measure and model. Up till now, two experiments have been performed to measure HHG based on this kind of field [11,19], while only few theoretical approaches have been developed [20–22]. One should note, however, that the interpretation of the authors of Ref. [11] remains controversial [23–25].

In our previous paper [14], in which we employed SFA to investigate the HHG by resonant plasmon field enhancement, the inhomogeneous vector potential field was defined in an approximated way starting from the homogeneous one. In the present paper, we improve our model even more by applying the same approximation directly to the inhomogeneous electric field rather than the potential. Subsequently, the vector potential is now derived from the electric field. In addition, we use an SFA based on saddle-point methods rather than a full numerical SFA approach to obtain the HHG spectra. The saddle-point methods lead to equations that can be directly related to the classical equations of motion of an electron in a laser field. As a result, they provide a space-time picture which gives us additional physical insight. In this work, we scrutinize the individual electron trajectories in comparison to their classical counterparts and demonstrate their contributions to the HHG spectra. In addition, since the imaginary part of the saddle-point equations can be related to the width of the potential barrier through which the electron tunnels, we examine the ionization probability of the electron for each trajectory.

This article is organized as follows. In Sec. II, we present the SFA transition amplitude for high-order harmonics, starting from common expressions based on homogeneous electric fields (Sec. II A) and, subsequently, by showing how we modify it for the case with nonhomogeneous fields (Sec. II B). In Sec. III, we discuss the saddle-point equations and analyze them in terms of quantum orbits in parallel to their classical counterpart electron trajectories. In the next section, Sec. IV, we present the HHG spectra based on the analysis given in Sec. III. Finally, in Sec. V, we summarize the paper and state our main conclusions.

II. THEORY

A. Transition amplitude

Generally, there are two main assumptions behind the SFA, namely (i) the influence of the laser field is neglected when the electrons are bound to their target atoms and (ii) the binding ionic potential is neglected when the electrons are in the continuum. As a result, the free electrons in the continuum are described by field-dressed plane waves, which are known as Volkov states [26,27].

1. Homogeneous fields

In the Lewenstein model [28], a well-established SFA-based method to model HHG, it is assumed that the laser electric field does not change with respect to the position in the region where the electron motion takes place. In this spatially homogeneous field, the SFA transition amplitude for HHG reads (in atomic units)

$$b_\Omega = i\int_{-\infty}^{\infty} dt \int_{-\infty}^{t} dt' \int d^3k d^*_{\rm rec}(\tilde{\mathbf{k}}(t)) d_{\rm ion}(\tilde{\mathbf{k}}(t')) \times e^{-iS(\Omega,\mathbf{k},t,t')} + \text{c.c.} \quad (1)$$

with the action

$$S_0(\Omega,\mathbf{k},t,t') = \int_{t'}^{t} \frac{[\mathbf{k}+\mathbf{A}(\tau)]^2}{2} d\tau + I_p(t-t') - \Omega t \quad (2)$$

and the prefactors

$$d_{\rm ion}(\tilde{\mathbf{k}}(t')) = \langle \tilde{\mathbf{k}}(t')|H_{\rm int}(t')|\phi_0\rangle, \quad (3)$$

$$d_{\rm rec}(\tilde{\mathbf{k}}(t)) = \langle \tilde{\mathbf{k}}(t)|O_{\rm dip}e_x|\phi_0\rangle. \quad (4)$$

Thereby, k, I_p, Ω, $H_{\rm int}(t')$, $O_{\rm dip}$, and e_x denote the drift momentum of the electron in the continuum, the ionization potential of the of the field-free bound state $|\phi_0\rangle$, the harmonic frequency, the interaction of the system with the laser field, the dipole operator, and the laser polarization vector, respectively. The vector potential $\mathbf{A}(t)$ of the laser electric field $E(t)$ is defined by

$$\mathbf{A}(t) = -\int_{-\infty}^{t} E(t')dt'. \quad (5)$$

Physically, Eq. (1) describes a process in which an electron, initially in a bound state $|\phi_0\rangle$ with energy I_p, interacts with the laser field by $H_{\rm int}(t')$ at the time t' and tunnels into a Volkov state $|\tilde{\mathbf{k}}(t)\rangle$. Subsequently, from time t' to t, it propagates in the continuum and is driven back by a laser field to its parent ion. At the time t, upon its return, this electron recombines with the core and emits high-harmonic radiation of frequency Ω. The second term in Eq. (1), which corresponds to the continuum-continuum transitions, can be ignored since it contributes very insignificantly to the transition amplitude of HHG (for details see Ref. [29]). The main drawback of SFA is that it is not gauge invariant. As a result, the matrix elements describing the ionization and recombination [i.e., Eqs. (3) and (4)] have different form in the length and velocity gauges. This comes from the fact that both the interaction Hamiltonian $H_{\rm int}(t')$ and the Volkov wave function $|\tilde{\mathbf{k}}(t)\rangle$ are not translationally invariant. The interaction Hamiltonian is given by $H^l_{\rm int}(t) = \mathbf{r}\cdot\mathbf{E}(t')$ and $H^v_{\rm int}(t) = [\mathbf{k}+\mathbf{A}(t')]/2$ in the length and velocity gauges, respectively. For the Volkov wave function, $\tilde{\mathbf{k}}(t) = \mathbf{k}+\mathbf{A}(t)$ in the length gauge and $\tilde{\mathbf{k}}(t) = \mathbf{k}$ in the velocity gauge. In this paper, we work in the length gauge and we assume that the electric field is linearly polarized along the x axis. Furthermore, we consider a hydrogenic $1s$ state for the field-free bound state $|\phi_0\rangle$.

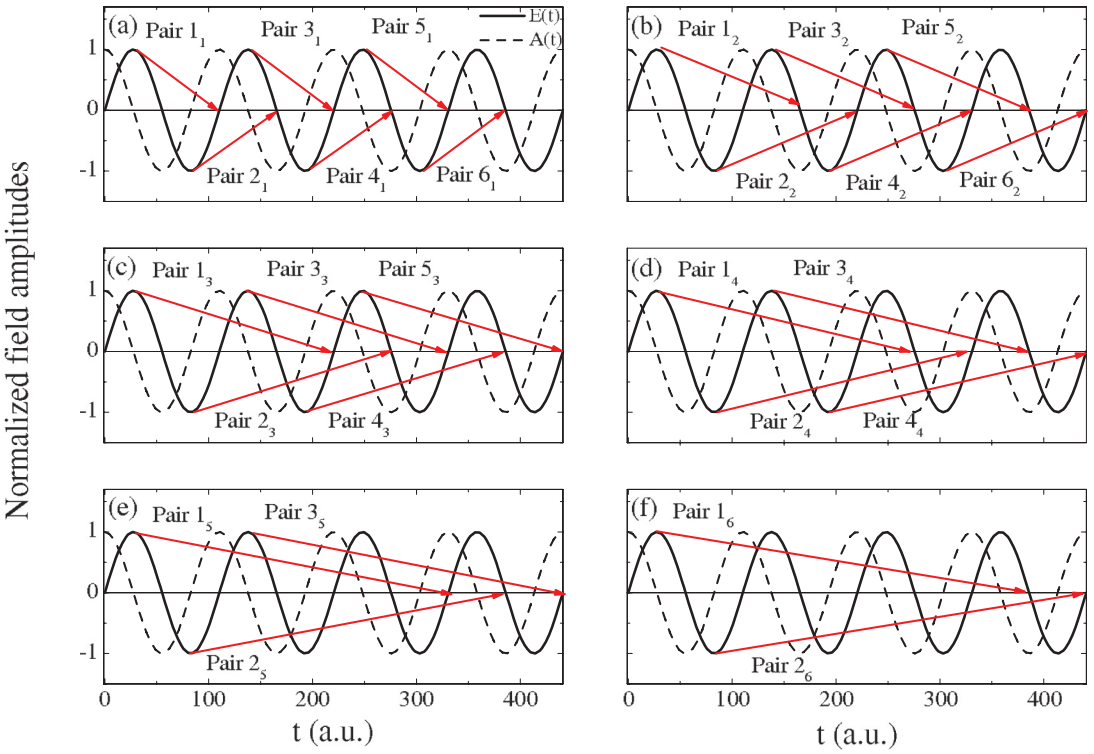

FIG. 1. (Color online) Schematic representation of the laser electric field $\mathbf{E}(t)$ and the corresponding potential field $\mathbf{A}(t)$ for a monochromatic field defined by $\mathbf{E}(t) = E_0 \sin(\omega t)e_x$, with four cycles. The arrow indicates the classical times around which the electrons leave to the continuum and return at the field crossing, approximately. The pairs of the orbits are indicated by the labels Pair$_n$, where n ranges from 1 to 8. Panels (a)–(f) represent the first, second, third, fourth, fifth, and sixth shortest pairs, respectively. The fields are normalized to $\mathbf{A}(t)/A_0$ and $\mathbf{E}(t)/E_0$, where A_0 and E_0 are the field amplitudes.

As a result, Eqs. (3) and (4) yield

$$d_{\text{ion}}(\widetilde{\mathbf{k}}(t')) \propto \frac{\widetilde{\mathbf{k}}(t')_x}{[\widetilde{\mathbf{k}}(t')^2 + \alpha^2]^3} E(t'), \tag{6}$$

$$d_{\text{rec}}(\widetilde{\mathbf{k}}(t)) \propto \frac{\widetilde{\mathbf{k}}(t)_x}{[\widetilde{\mathbf{k}}(t)^2 + \alpha^2]^3}. \tag{7}$$

2. *Nonhomogeneous fields*

We will now consider a case in which that assumption made in Sec. II A1 is not valid any more and the laser field has a spatially inhomogeneous character when the HHG process takes place. Before discussing the nonhomogeneous case, we examine how the action of the SFA is connected to classical electron trajectories for the homogeneous field. The laser potential V_L due to the laser field $E(t)$ is defined as

$$V_L = xE(t), \tag{8}$$

and the Newton equation of motion for an electron in this field is given by

$$\ddot{x}(t) = -\nabla_x V_L. \tag{9}$$

In here, the force is equal to (minus) the laser electric field [i.e., $\ddot{x}(t) = -E(t)$]. In the SFA, the action is defined in terms of the vector potential field $A(t)$ given by Eq. (5), which is the counterpart of the velocity $\dot{x}(t)$.

For the inhomogeneous case the electric field now has the form $E(t,x)$ and the laser potential is $V_L = xE(t,x)$. Thus, the Newton equation of motions become

$$\ddot{x}(t) = -x\nabla_x E(t,x) - E(t,x). \tag{10}$$

From Eq. (10), it is clear that $\ddot{x}(t) \neq -E(t,x)$. Therefore, the potential field $A(t)$ of the SFA action should correspond to the integration of $\ddot{x}(t)$ with respect to t.

If the spatial dependence of the laser electric field is perturbative and linear with respect to position, then the field can be approximated as

$$E(t,x) \simeq E(t)(1 + \epsilon x), \tag{11}$$

where $\epsilon \ll 1$ is a parameter that characterizes the strength of the inhomogeneity.

Indeed, the above approximation corresponds to the first term of the actual field of a plasmonic nanostructure with spherical shape [30]. By substituting Eq. (11) into Eq. (10), we have

$$\ddot{x}(t) = -E(t)[1 + 2\epsilon x(t)]. \tag{12}$$

This is the effective laser electric field that the electron feels along the trajectory $x(t)$, which describes its motion in the continuum. We will call it the electron trajectory effective electric field.

Classically, the electron trajectory can be found by solving Eq. (12). In here, we solve it by applying the Picard iteration [31] method and restrict ourselves to the first order (for more details see Ref. [14]). Based on the condition that the electron starts its movement at the origin with zero velocity

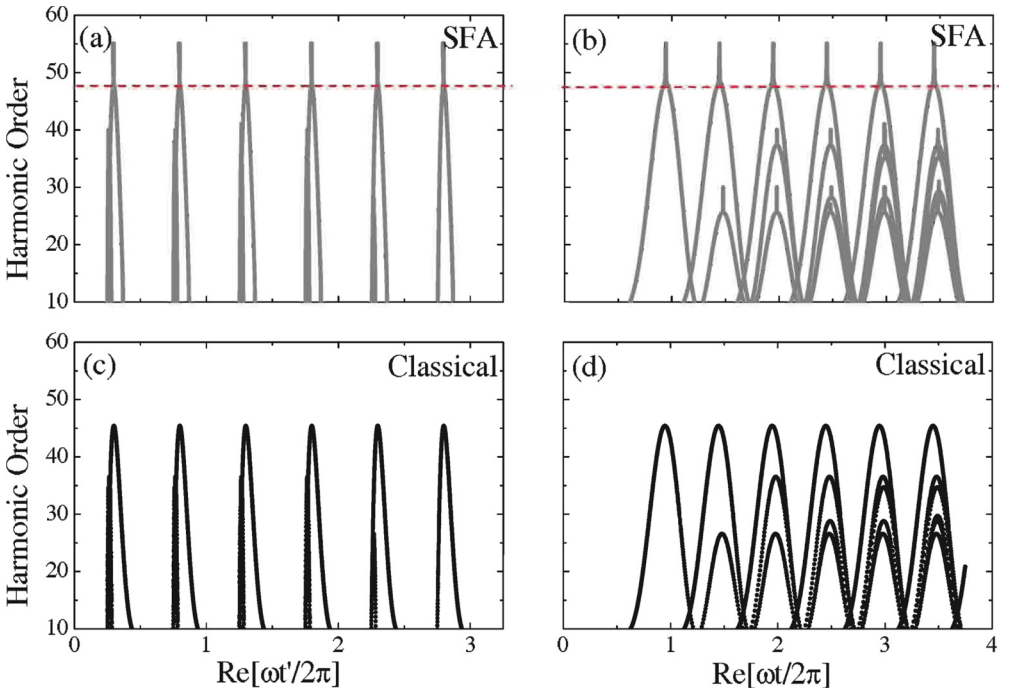

FIG. 2. (Color online) Dependence of harmonic order on the release time t' and the recombination time t of the electron for all given pairs in Fig. 1 and for the homogeneous field ($\epsilon = 0$). We consider a hydrogen atom, for which the ground-state energy is $I_p = 0.5$ a.u., in a linearly polarized, monochromatic field of frequency $\omega = 0.057$ a.u. and intensity $I = 3 \times 10^{14}$ W/cm^2. Panels (a) and (b) give the harmonic order as a function of the ionization and recombination times of the SFA model, respectively, while panels (c) and (d) depict the the harmonic order in terms of ionization and recombination times of the classical calculations, respectively. The red dashed lines correspond to the harmonic cutoff.

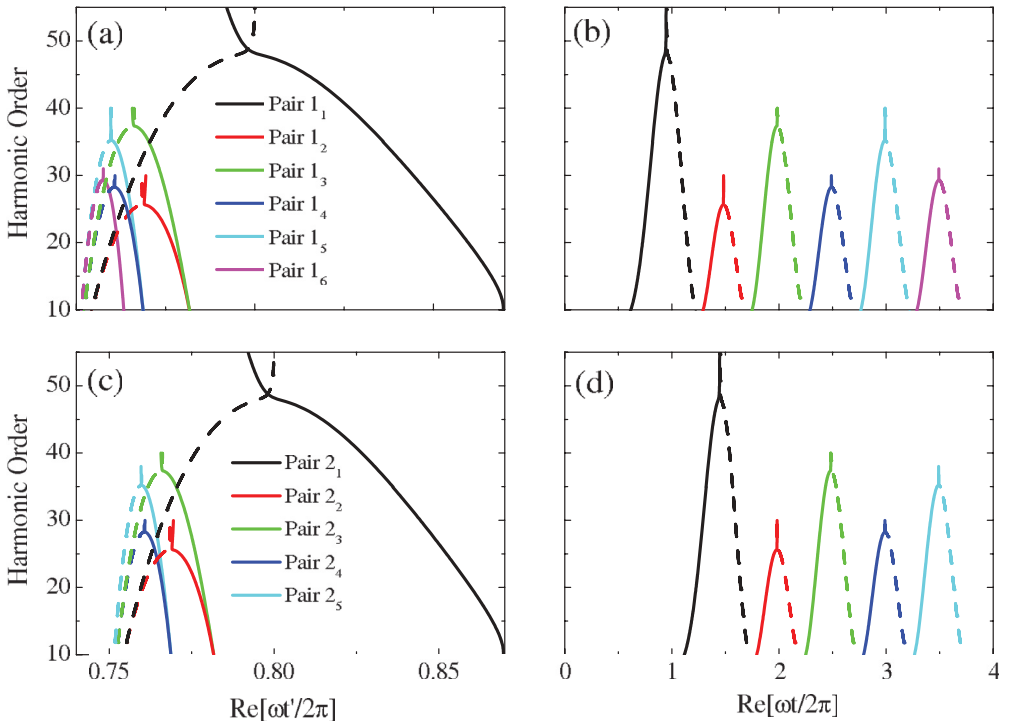

FIG. 3. (Color online) SFA harmonic order as a function of the real part of the release time t' and the recombination time t of the electron for the same parameters as in Fig. 2, but for pairs 1_n and 2_m (where $n = 1$–6 and $m = 1$–5) of Fig. 1. Panels (a) (from right to left $1_1 \rightarrow 1_6$) and (b) (from left to right $1_1 \rightarrow 1_6$) give the ionization and recombination times of pairs 1_n, respectively. Panels (c) (from right to left $2_1 \rightarrow 2_5$) and (d) (from left to right $2_1 \rightarrow 2_5$) depict the ionization and recombination times of pairs 2_m, respectively. The dashed and solid lines correspond to the long and the short orbits, respectively.

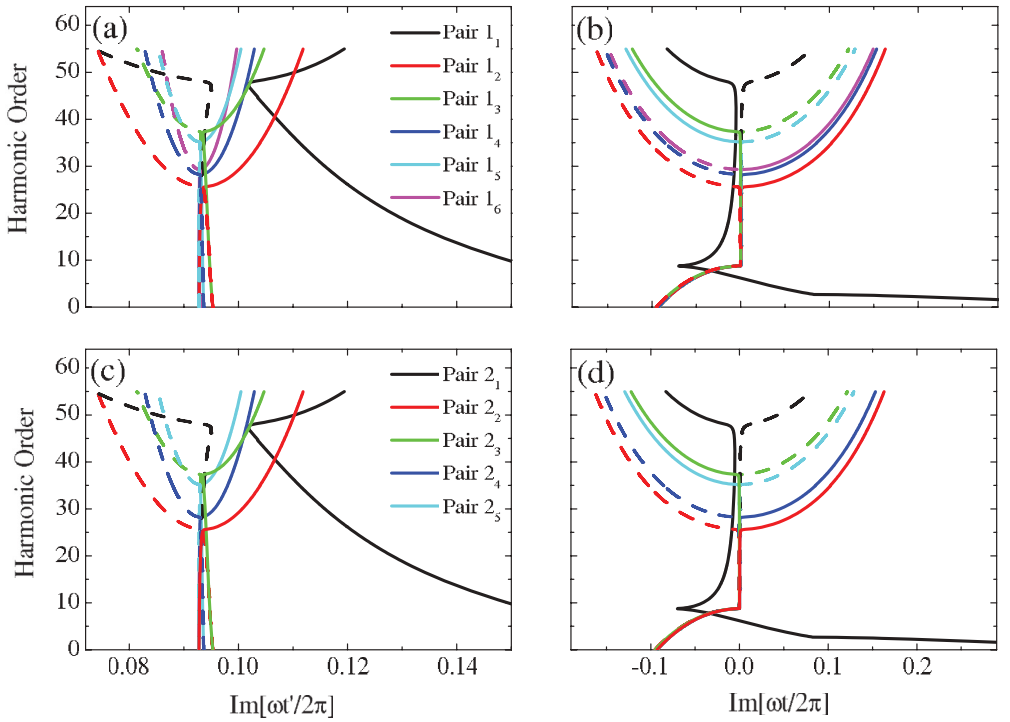

FIG. 4. (Color online) SFA harmonic order as a function of the imaginary part of the release time t' and the recombination time t of the electron for the same parameters as in Fig. 2, but for pairs 1_n and 2_m (where $n = 1$–6 and $m = 1$–5) of Fig. 1. Panels (a) and (b) give the ionization and recombination times of pairs 1_n, respectively, and panels (c) and (d) depict the ionization and recombination times of pairs 2_m, respectively. The dashed and solid lines correspond to the long and the short orbits.

[i.e., $x(0) = 0$ and $\dot{x}(0) = v(0) = 0$], we obtain

$$x(t) = \beta(t) - \beta(t_0) - A(t_0)(t - t_0), \tag{13}$$

with $\beta(t) = \int_0^t dt' A(t')$. In addition we assume that at time t_0 the potential field is zero; thus

$$x(t) = \int^t dt' A(t'). \tag{14}$$

By using Eqs. (5), (12), and (14), the effective vector potential along the electron trajectory $A_{\rm tr}(t)$ reads

$$A_{\rm tr}(t) = A(t) + 2\epsilon A_c(t), \tag{15}$$

where

$$A_c(t) = \int^t dt'' A(t'') - \int^t dt'' A^2(t''). \tag{16}$$

The next step is to modify the general expression of the transition amplitude (1) for the HHG to include the above-defined inhomogeneous field. Consequently, we have to replace the electric field and vector potential by Eqs. (11) and (15), respectively. As a result, the modified action yields

$$S(\Omega,\mathbf{k},t,t') = S_0(\Omega,\mathbf{k},t,t') + 2\epsilon \int_{t'}^t A_c(\tau)[\mathbf{k} + \mathbf{A}(\tau)]d\tau + 2\epsilon^2 \int_{t'}^t A_c^2(\tau)d\tau, \tag{17}$$

where $S_0(\Omega,\mathbf{k},t,t')$ is defined in Eq. (2).

B. Saddle-point equations

The transition amplitude (1) can be computed either numerically or by using the saddle-point method [32,33]. In here, we employ the latter procedure since the solutions of the saddle-point equations are directly related to the classical trajectories. Thus, it allows us to investigate the quantum orbits in comparison to the classical trajectories as well as demonstrating their contributions to the cutoff and yield of the HHG. This method requires obtaining the saddle points where the action (17) is stationary [i.e., for which $\partial_t S(\Omega,\mathbf{k},t,t') = \partial_{t'} S(\Omega,\mathbf{k},t,t') = \partial_k S(\Omega,\mathbf{k},t,t') = 0$]. In this paper, we use a specified steepest descent method called uniform approximation to take care of those saddle points which are not well separated (for a detailed discussion see Ref. [34]). The stationary conditions upon t,t' and k lead to the saddle-point equations

$$[\mathbf{k} + \mathbf{A}(t')]^2 - 2\epsilon\lambda(t') = -2I_p, \tag{18}$$

$$\int_{t'}^t d\tau[\mathbf{k} + \mathbf{A}(\tau)] + 2\epsilon\eta(\tau) = 0, \tag{19}$$

and

$$\Omega = \frac{[\mathbf{k} + \mathbf{A}(t)]^2}{2} + I_p + 2\epsilon\lambda(t), \tag{20}$$

with

$$\lambda(t) = A_c(t)[\mathbf{k} + \mathbf{A}(t)] + \epsilon A_c^2(t), \tag{21}$$

and

$$\eta(\tau) = \int_{t'}^t A_c(\tau)d\tau. \tag{22}$$

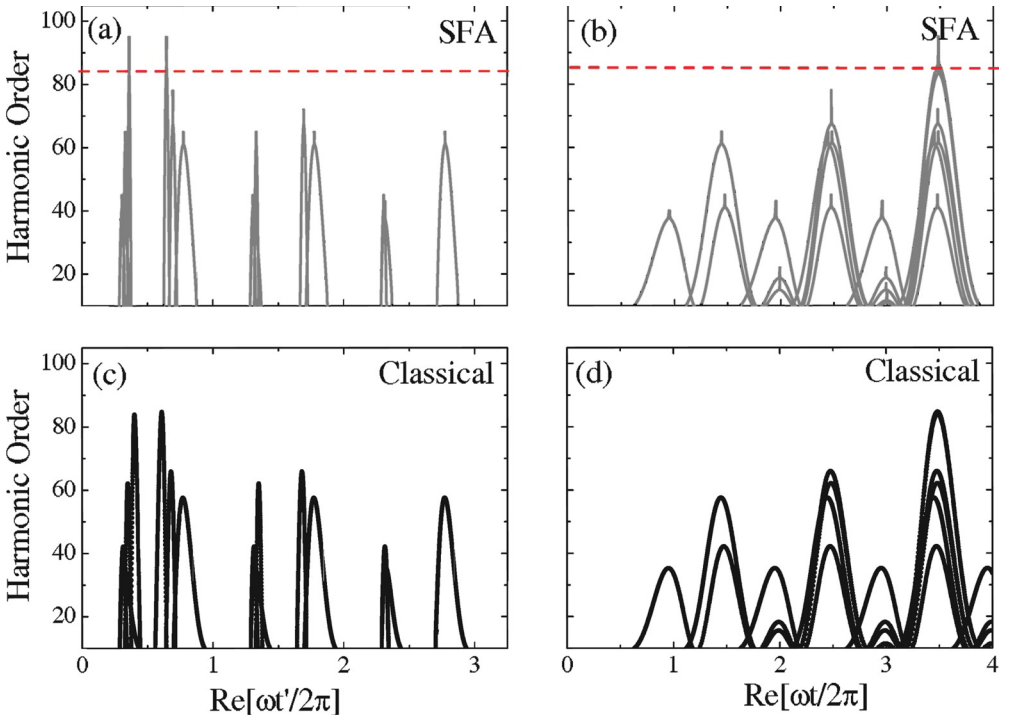

FIG. 5. (Color online) Dependence of harmonic order on the release time t' and the recombination time t of the electron for all given pairs in Fig. 1, for a nonhomogeneous field with $\epsilon = 0.003$. We consider hydrogen atoms for which the ground-state energy is $I_p = 0.5$ a.u. in a linearly polarized, monochromatic field of frequency $\omega = 0.057$ a.u. and intensity $I = 3 \times 10^{14}$ W/cm^2. Panels (a) and (b) give the ionization and recombination times of the SFA model, respectively, while panels (c) and (d) depict the ionization and recombination times of the classical calculations, respectively. The red dashed lines correspond to the harmonic cutoff.

Equation (18) expresses the conservation law of energy for the electron tunnel ionized at the time t'. Equation (19) guarantees that the electron returns to its parent ion as well as constraining the intermediate momentum of the electron. Finally, Eq. (20) gives the energy conservation of the electron at the time t, when upon its return it recombines with the core and releases a high frequency photon Ω.

The terms $\lambda(t')$, $\eta(t)$, and $\lambda(t)$ in Eqs. (18)–(20), respectively, emerge from the nonhomogeneous character of the laser field and they vanish for the homogeneous case [i.e., when $\epsilon = 0$]. For the homogeneous case, the solutions of the saddle-point equations are generally complex since Eq. (18) admits no real solutions unless $I_p \to 0$. This is a consequence of the fact that tunneling has no classical counterpart. For the inhomogeneous case, however, it is not very upfront to constrain the limit, in which the solutions of Eq. (18) are real. Nevertheless, in here, ϵ is a very small parameter and the electron will most likely reach the continuum with tunnel ionization. Thus, the solutions of these saddle-point equations are still expected to be complex. In addition, the maximum kinetic energy that the electron gains in the continuum is no longer $3.17U_p$, where $U_p = E_0^2/(4\omega^2)$ is the ponderomotive energy. In fact, it depends on the nonhomogeneous character of the field [i.e., of ϵ and $A_c(t)$]. For positive A_c, the electron gains energy, depending on the value of the ϵ, larger than $3.17U_p$, while for the negative A_c it would be below the conventional value.

We now examine the drift momentum $\mathbf{k}$ of the electron at the time of the tunneling Eq. (18). For that, we consider the limit $I_p \to 0$, where the electron reaches the continuum with zero kinematical momentum. As a result, Eq. (18) yields

$$\mathbf{k} = -A(t') + \epsilon A_c(t')(1 \mp \sqrt{3}). \tag{23}$$

Unlike the homogeneous case, where $\mathbf{k} = -A(t')$, in here, $\mathbf{k}$ has two different solutions with one exceeding and the other lowering the homogeneous drift momenta. The strength of the inhomogeneity ϵ and the shape of the $A_c(t')$ are the responsible of this deviation.

III. RESULTS

A. Quantum orbits

In this section, we investigate the role of individual trajectories to the HHG cutoff for the nonhomogeneous case by performing a quantum-orbit analysis of the problem. The concept of the quantum orbits is based on the fact that the solutions of the saddle-point equations can be related to the classical trajectories of the electron and, in addition, to obtain information on quantum aspects such as tunneling and interference. To get a better insight into the nonhomogeneous case, we employ a monochromatic field with $E(t) = E_0 \sin(\omega t)e_x$, where e_x is the polarization vector along the x axis. By using the relationship defined in Eq. (5) and applying some trigonometric identities, the laser effective electric field (12) and effective potential field (15) along the electron trajectory read

$$E_{\rm tr}(t) = E_0 \sin(\omega t)[1 + 2\epsilon \sin(\omega t)/\omega^2], \tag{24}$$

$$A_{\rm tr}(t) = A_0 \cos(\omega t) + 2\epsilon A_c(t), \tag{25}$$

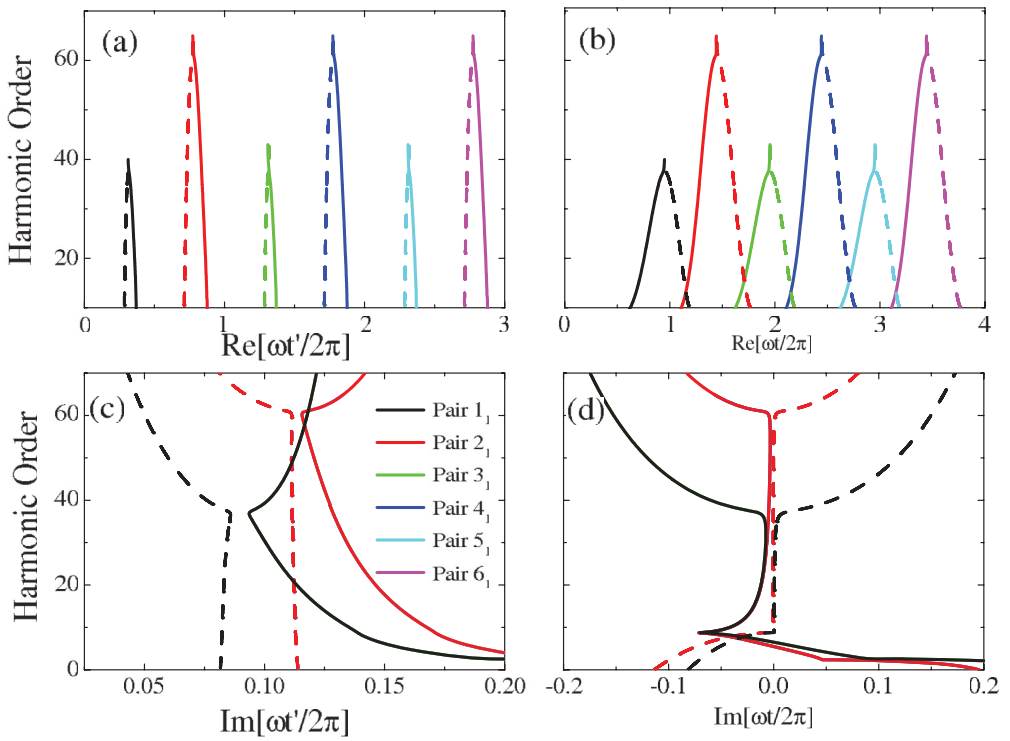

FIG. 6. (Color online) Dependence of harmonic order on the release time t' and the recombination time t of the electron for the same parameters as in Fig. 5, but for pairs n_1 (where $n = 1$–6) of Fig. 1. Panels (a) and (c) (from left to right $1_1 \rightarrow 6_1$) depict the real part of the release and recombination times, respectively, while panels (c) and (d) show the imaginary part of the ionization and recombination times of pairs n_1, respectively. The dashed and solid lines correspond to the long and the short orbits.

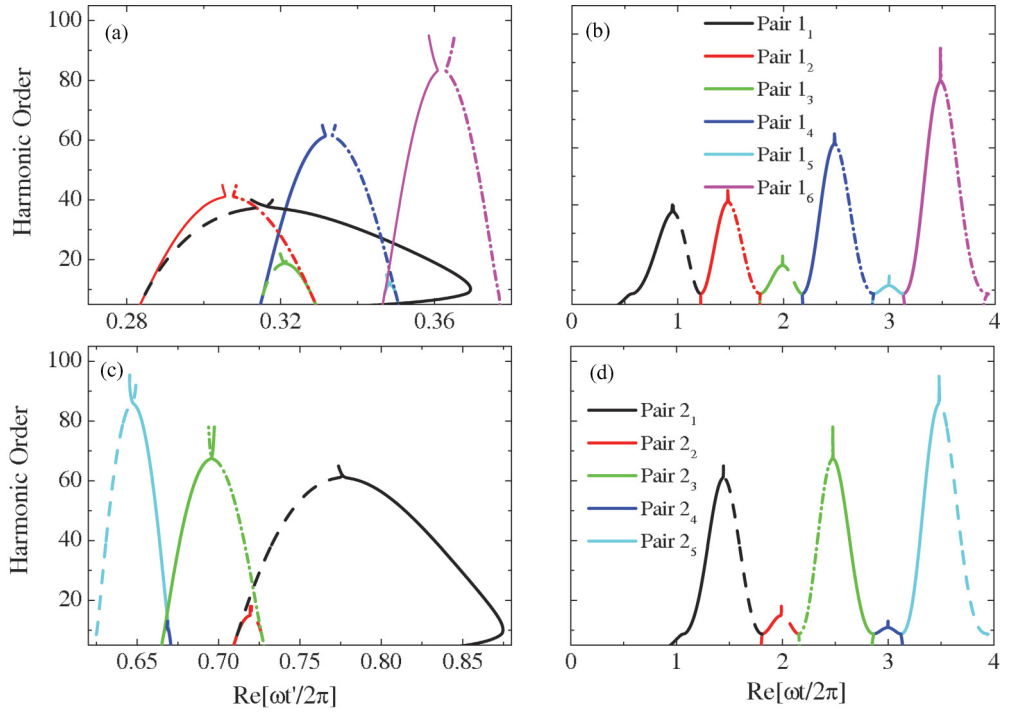

FIG. 7. (Color online) SFA harmonic order as a function of the real part of the release time t' and the recombination time t of the electron for the same parameters as in Fig. 5, but for pairs 1_n and 2_m (where $n = 1$–6 and $m = 1$–5) of Fig. 1. Panels (a) and (b) (from left to right $1_1 \rightarrow 1_6$) give the ionization and recombination times of pairs 1_n, respectively, and panels (c) and (d) (from left to right $2_1 \rightarrow 2_5$) depict the ionization and recombination times of pairs 2_m, respectively. The dashed and solid lines correspond to the long and the short orbits, while the pairs with dot dashed lines do not have the well-known short and long pairs.

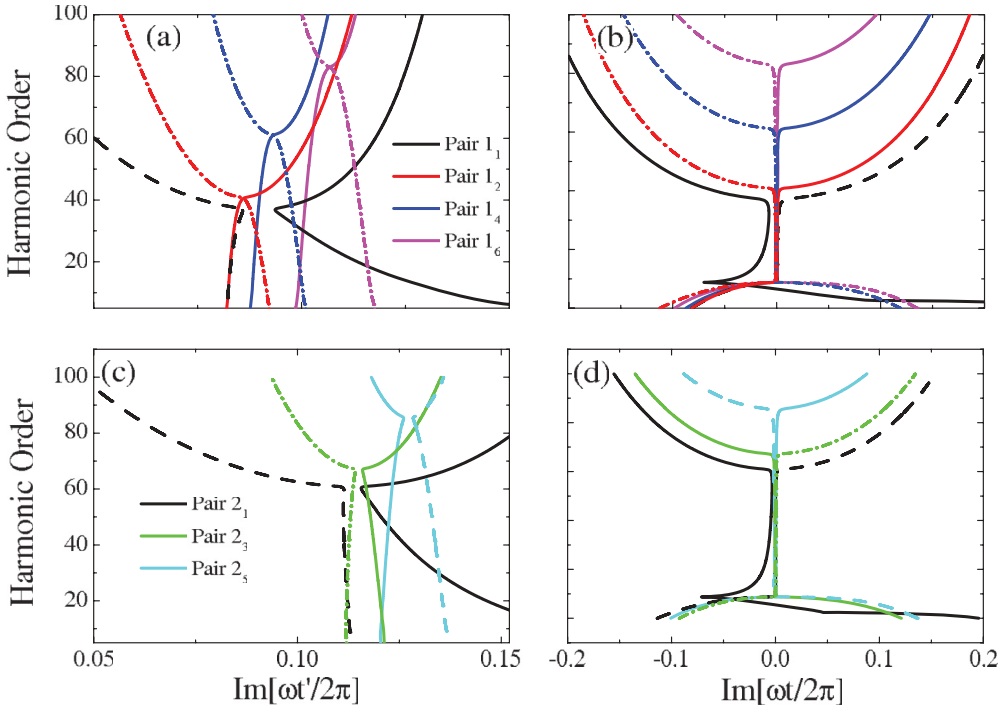

FIG. 8. (Color online) SFA harmonic order as a function of the imaginary part of the release time t' and the recombination time t of the electron for the same parameters as in Fig. 5, but for pairs 1_n and 2_m (where $n = 1,2,4,6$ and $m = 1,3,5$) of Fig. 1. Panels (a) and (b) give the ionization and recombination times of pairs 1_n, respectively, and panels (c) and (d) depict the ionization and recombination times of pairs 2_m, respectively. The dashed and solid lines correspond to the long and the short orbits, while the pairs with dot dashed lines do not have the well-known short and long pairs.

respectively, where $A_0 = E_0/\omega$ and

$$A_c(t) = A_0^2 \sin(\omega t)/4\omega - A_0^2 t/2. \tag{26}$$

In terms of the pondermotive energy of the homogeneous field, the drift momentum of Eq. (23) yields

$$\mathbf{k} = -2\sqrt{U_p}\cos(\omega t') + \epsilon\left(\frac{U_p}{\omega}\sin(\omega t') - 2U_p t'\right)(1 \mp \sqrt{3}). \tag{27}$$

Based on the above equations, we solve the saddle-point equations defined in Eqs. (18) through (20) in terms of the ionization t' and recombination t times. For a more close analysis, we restrict ourselves just to the solutions of the first four cycles of our defined monochromatic field, as shown in Fig. 1. Classically, it is most probable that the electron ionizes at the electric field maxima and returns to its parent's ion at the electric field crossings. Figures 1(a)–1(d) depict the cases when the electron leaves at the field maxima and returns to the core at time about π, 2π, 3π, and 4π later, respectively.

In Fig. 2, we plot the the harmonic order as a function of the real parts of the ionization t' and recombination t times for the case with $\epsilon = 0$ [Figs. 2(a) and 2(b), respectively]. In this figure, in comparison to the SFA model, we also present the classical solutions of t' and t [Figs. 2(c) and 2(d), respectively]. From Fig. 2 it is clear that the SFA resembles the classical calculations. Apart from that, both calculations show that the ionization and recombination times corresponding to each cycle are identical.

In Fig. 3, we isolate those solutions and plot the harmonic order in terms of the real parts of ionization and recombination times by considering the case when the electron leaves the atom at the times around $\pi/2$ and returns to the core at the times $n\pi$ ($n = 2,3,4,5$) [Figs. 3(a) and 3(b) for t' and t, respectively] and the case when the electron leaves the atom at the times around π and returns to the core at $n\pi$ ($n = 3,4,5$) [Figs. 3(c) and 3(d) for t' and t, respectively]. For a given harmonic, there is always a shorter (solid line) and a longer (dashed line) travel time for the electron in the continuum, corresponding to the long and short trajectories of the pair. Such pairs of orbits coalesce at the maximally allowed harmonic energies (i.e., at the cutoff). In here, the shortest orbits (i.e., the one that the electron leaves at the field maxima and returns at around time π later) have the largest cutoff, at harmonic 47ω. It means that these pairs of orbits lead the cutoff of the HHG spectra, while the other pairs produce harmonics with lower energies.

In Fig. 4, we present the imaginary parts of ionization and recombination times of the pairs shown in Fig. 3. Figures 4(a) and 4(b) depict the t' and t for $n\pi$ ($n = 2,3,4,5$), respectively. Figures 4(c) and 4(d) demonstrate the t' and t for $n\pi$ ($n = 3,4,5$), respectively. For the recombination times, Im[t] essentially vanishes between the harmonic order for which the real parts Re[t] coalesce. Physically, this means that, in this region, the recombination is classically allowed. Beyond this region, Im[t] increases abruptly, which indicates that the classically forbidden region has been reached. On the other hand, the imaginary part Im[t'] of the start time of the electron is always nonvanishing. This is due to the fact that the tunneling

has no classical counterpart. These results show that both the imaginary and real parts of the tunneling and recombination times for pairs 1_n (where $n = 1$–6) and 2_m ($m = 1$–5) given in Fig. 1 are similar.

Now we move to the nonhomogeneous case and consider $\epsilon = 0.003$. In Fig. 5, we demonstrate the harmonic order as function of the real parts of the ionization t' and recombination t times for such a case. Like above, the SFA [Figs. 5(a) and 5(b) for t' and t, respectively] resembles the classical calculations [Figs. 5(c) and 5(d) for t' and t, respectively]. The general harmonic cutoff is extended in comparison to the homogeneous case, but the trajectories do not follow the same symmetry as shown in Fig. 2.

To closely examine the orbits, we plot the harmonic order of the shortest pairs [i.e., pairs $n\pi$ ($n = 1$ to 5)], in terms of ionization and recombination times (Fig. 6). Figures 6(a) and 6(c) represent the real and the imaginary parts of t', respectively, and Figs. 6(b) and 6(d) represent the real and the imaginary parts of t, respectively. Unlike the homogeneous case, these pairs do not lead to the same cutoff. For the pairs corresponding to the electron leaving at the field maxima [Fig. 1(a)], the cutoff is at around harmonic 38ω, while for the pairs corresponding to the electron leaving at the field minima the cutoff is at around harmonic 60ω. These results come from the fact that, for a given harmonic, the electron may tunnel with two possible momenta given by Eq. (27). It appears that the electron has larger momenta if it tunnels from the minima of the field and smaller momenta if it tunnels from the maxima of the field.

Figures 7 and 8 demonstrate the dependence of harmonic order on the real and imaginary parts of ionization and recombination times, respectively, by considering the case when the electron leaves the atom at the times around $\pi/2$ and returns to the core at the times $n\pi$ ($n = 2,3,4,5$) [Figs. 7(a) and 8(a) for t' and Figs. 7(b) and 8(b) for t] and the case when the electron leaves the atom at the times around π and returns to the core at $n\pi$ ($n = 3,4,5$) [Figs. 7(c) and 8(c) for t' and Figs. 7(d) and 8(d) for t]. For the dominant pairs the cutoff becomes larger as we move from shorter pairs to the longer pairs. For instance, pair 1_1, which is associated to the electron which leaves at the times around $\pi/2$ and recombined at the times 2π, has a cutoff at harmonic 38ω, while the cutoff of pair 1_6, which is associated to the electron which leaves at the times around $\pi/2$ and recombined at the times 5π, is at harmonic 80ω. In contrast to the homogeneous case, in here, the pairs which are associated with the electron which recombined a few cycles later from the time of its ionization lead to the larger cutoff. Furthermore, for some of the pairs (shown with dot-dashed lines) like pair 1_6 and pair 2_3 the conventional concept of the short orbit, in which the electron leaves a bit later and returns a bit earlier, and the long orbit, in which the electron leaves a bit earlier and returns a bit later, does not have any meaning. In fact, for these pairs, if the electron leaves a bit early then return a bit early and if it leaves a bit later then returns a bit later.

In addition, the ionization time of the electron has even more interesting behavior as shown in Fig. 9. For pairs 1_n and pairs 2_m (where $n = 1$–6 and $m = 1$–5), the ionization time t' moves toward π as n and m become larger, until both solutions collapse on each other as is demonstrated in

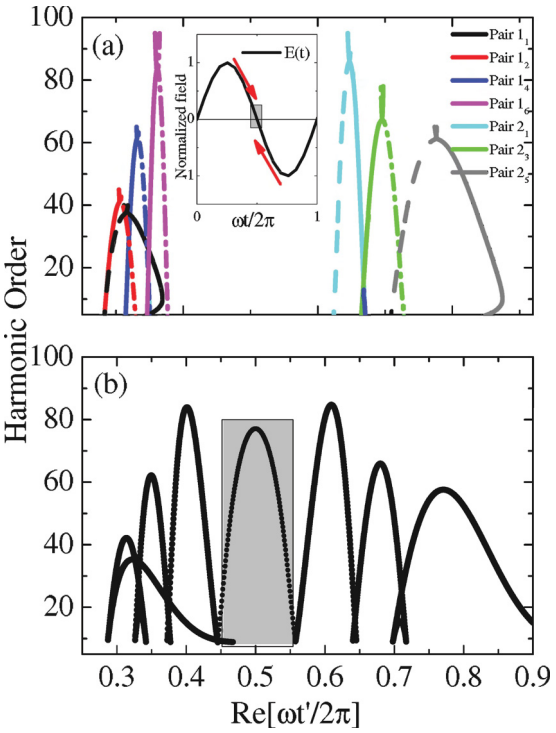

FIG. 9. (Color online) Harmonic order as a function of the release time t' of the electron for the same parameters given in Fig. 5, but for pairs 1_n and 2_m (where $n = 1,2,4,6$ and $m = 1,3,5$) of Fig. 1. Panel (a) gives the real part of the release times based on SFA, while panel (b) depicts the classical ionization times of these pairs. The dashed and solid lines correspond to the long and the short orbits, while the pairs with dot dashed lines do not have the well-known short and long pairs.

Fig. 9. Figure 9(a) depicts the SFA calculation while Fig. 9(b) represents the classical calculations. For the SFA model, the ionization time as a function of n and m moves more slowly toward π in comparison to the classical calculations. In the classical calculations, the collapse at $t' = \pi$ is associated to the pairs 1_7 and 2_6. In the SFA model, however, this collapse is not exactly centered at around $t' = \pi$, instead it manifests itself by collapsing to its previous pair. On the other hand, both SFA and classical models give the same cutoff. It means the SFA will give a reliable HHG spectra while its yields will be affected quantitatively, which would not be a problem since SFA has the same limitation even for the homogeneous fields.

In Fig. 10, we demonstrate the harmonic order as a function of the real parts of the ionization t' and recombination t times for $\epsilon = 0.005$. Figures 10(a) and 10(c) depict the t' and Figs. 10(b) and 10(d) show t, for SFA and classical models, respectively. The SFA calculations are in good agreement with the classical model. In here, the general cutoff extends to the larger harmonic. In fact for the shortest pairs, the cutoff is at harmonic 70ω and for the longest allowed pairs the cutoff extends to harmonic 92ω. In comparison to the case with $\epsilon = 0.003$, for the shortest pairs (1_n with $n = 6$), the cutoff from the maxima and the minima of the field shift toward lower (harmonic 32ω) and higher harmonic (harmonic 70ω) as demonstrated in Fig. 11.

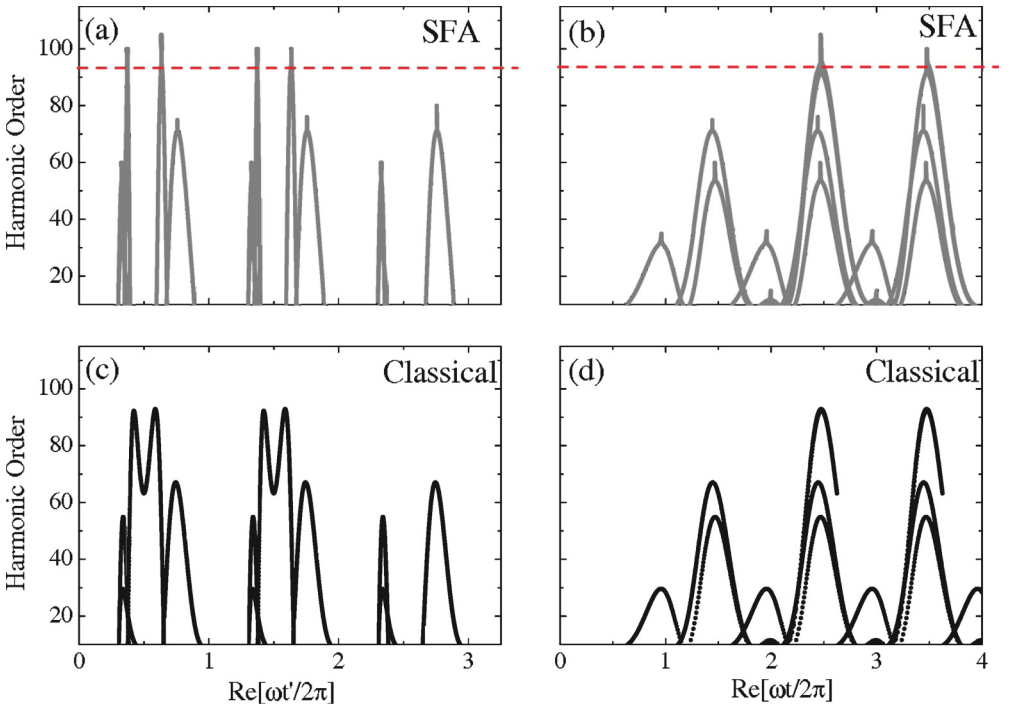

FIG. 10. (Color online) Dependence of harmonic order on the release time t' and the recombination time t of the electron for all given pairs in Fig. 1, for a nonhomogeneous field with $\epsilon = 0.005$. We consider hydrogen atoms for which the ground-state energy is $I_p = 0.5$ a.u. in a linearly polarized, monochromatic field of frequency $\omega = 0.057$ a.u. and intensity $I = 3 \times 10^{14}$ W/cm^2. Panels (a) and (b) give the ionization and recombination times of the SFA model, respectively, while panels (c) and (d) depict the ionization and recombination times of the classical calculations, respectively. The red dashed lines correspond to the harmonic cutoff.

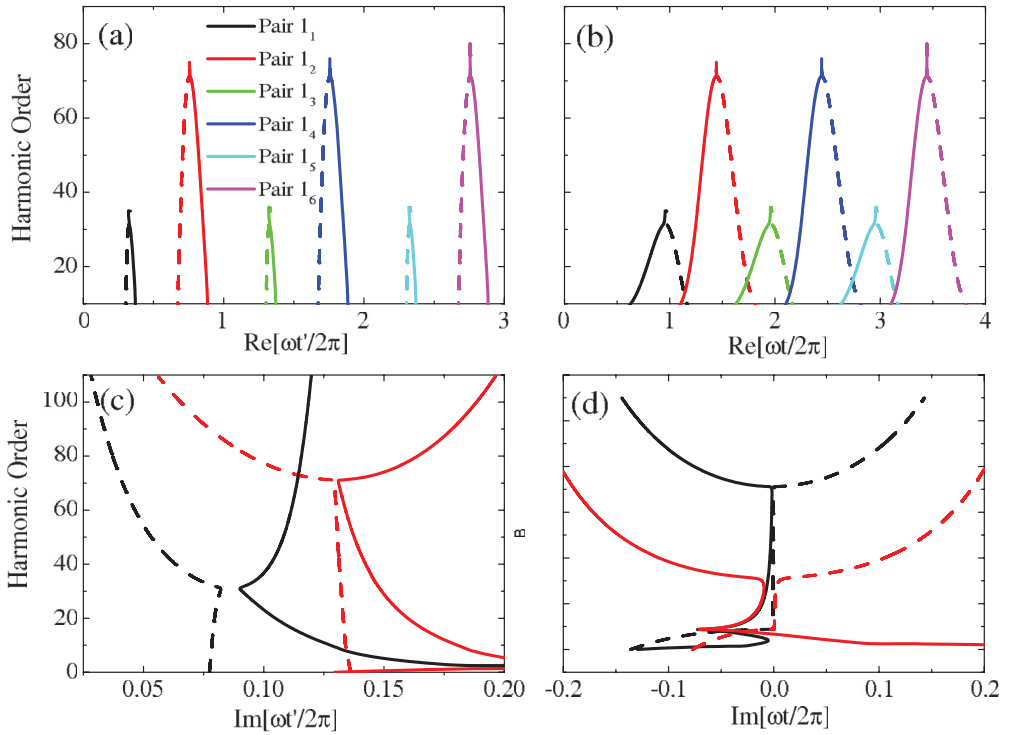

FIG. 11. (Color online) Dependence of harmonic order on the release time t' and the recombination time t of the electron for the same parameters as in Fig. 10, but for pairs 1_n (where $n = 1$–6) of Fig. 1. Panels (a) and (b) (from left to right $1_1 \rightarrow 1_6$) depict the real part of the release and recombination times, respectively, while panels (c) and (d) show the imaginary part of the ionization and recombination times of pairs 1_n, respectively. The dashed and solid lines correspond to the long and the short orbits, respectively.

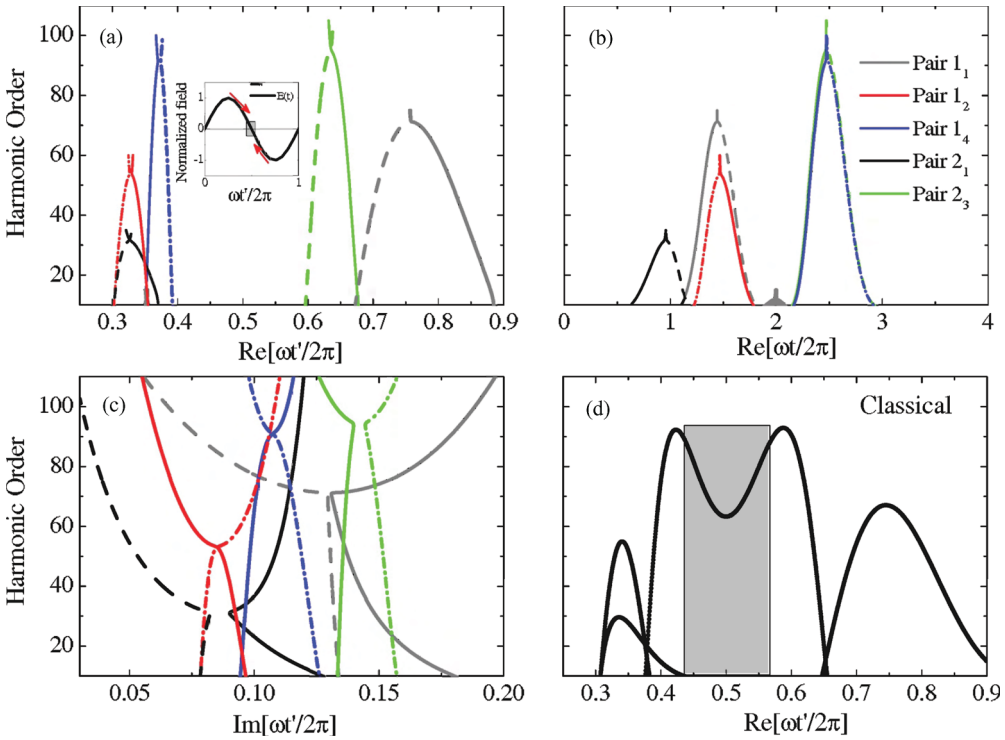

FIG. 12. (Color online) Harmonic order as a function of the release time t' and the recombination time t of the electron for the same parameters as in Fig. 5, but for pairs $1_1, 1_2, 1_4, 2_1$, and 2_3 of Fig. 1. Panels (a) and (b) give the real part of the release and recombination times of pairs, respectively, while panel (c) shows their imaginary parts. Panel (d) depicts the classical ionization times of these pairs. The dashed and solid lines correspond to the long and the short orbits, while the pairs with dot-dashed lines do not have the well-known short and long pairs.

Furthermore, the collapse of the pairs from maximum and minimum of a given cycle happens even faster as shown in Fig. 12. As we discussed above for $\epsilon = 0.003$, the collapse occurs at pairs 1_7 and 2_6, while in here it is at pairs 1_4 and 2_3. It means that, as the field becomes more inhomogeneous (i.e., larger values of ϵ), the electron does not return to the core if it follows the longer trajectories.

We verified, without showing it here, that for larger values of ϵ (like $\epsilon = 0.02$) even the longer trajectory of the shortest pairs does not lead to the return of the electron to the core. Despite the fact that our model does not accommodate such large values of ϵ, it suggests that for the strong inhomogeneous field just the shortest trajectories will lead to recombination process. In fact, our TDSE calculations [22], which based on the actual nonhomogeneous field generated in the confined region of bow-tie nanostructures, show that the shortest trajectories rather than longest are contributing to the HHG spectra.

B. Spectra

In this section, we compute HHG spectra with Eq. (1) using the saddle-point method developed in Sec. II B. Figure 13 presents HHG spectra for the case with $\epsilon = 0.003$. The spectra with green and blue colors represent the contributions from the shortest pairs with smaller cutoff (i.e., pairs $1_1, 1_3$, and 1_5) and the shortest pairs with largest cutoff (i.e., pairs $1_2, 1_4$, and 1_6), while the red color demonstrates the contributions from all other orbits given in Fig. 1. For all three cases, the HHG cutoffs are in good agreement with the trajectories represented in the previous section. The third case, which corresponds to the longest pairs, leads to the largest cutoff. This is expected since for these pairs the electron has more time to accelerate

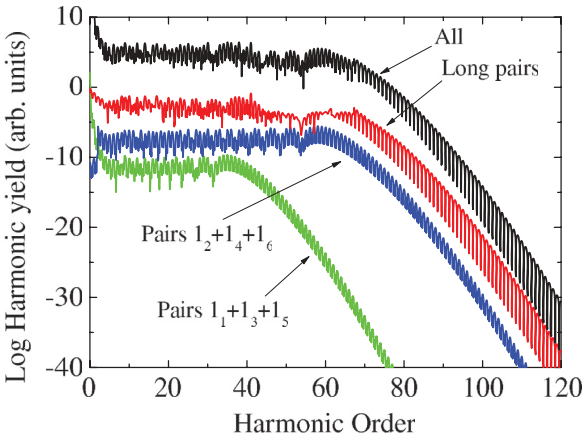

FIG. 13. (Color online) High-order harmonic spectra for hydrogen atoms ($I_p = 0.5$ a.u.) and interacting with a monochromatic field of frequency $\omega = 0.057$ a.u. and intensity $I = 3 \times 10^{14}$ W/cm^2 for the case with $\epsilon = 0.003$. Green and blue colored spectra show the contributions from the shortest pairs with smaller cutoff (i.e., pairs $1_1, 1_3$, and 1_5) and the shortest pairs with largest cutoff (i.e., pairs $1_2, 1_4$, and 1_6), while the red color demonstrates the contributions from all other orbits. Black colored spectra shows the total contributions from all pairs given in Fig. 1. For clarity, all the HHG spectra are scaled.

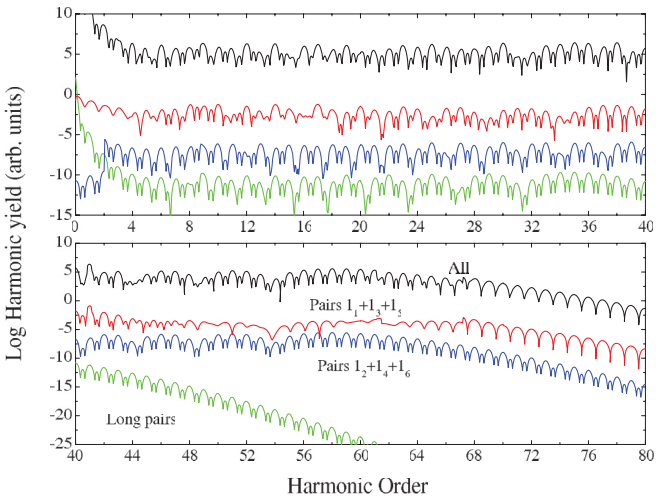

FIG. 14. (Color online) Zooming into the HHG spectra given in Fig. 13.

in the field and return to the core with higher energy. On the other hand, for these pairs, the wave packet spreads too much in the continuum. Therefore, they lead to a harmonic with lower yields. For the first two cases, which correspond to the shortest pairs, the harmonic yields will be large for both the cases (i.e., the one that has the largest and smallest cutoffs). The spectra with the black color shows the total contributions (i.e., from all the pairs given in Fig. 1).

We now zoom into the spectra of Fig. 13 to examine more closely the harmonic generated from these sets of pairs (Fig. 14). Up to harmonic 40ω, the shortest pairs with lower cutoff (1_1,1_3, and 1_5) give the shape of the total spectra and from harmonic 40ω to 64ω the shortest pairs with higher cutoff (1_2,1_4, and 1_6) dominate the shape of the total spectra. For the higher harmonic the rest of the pairs lead to the shape of the total spectra.

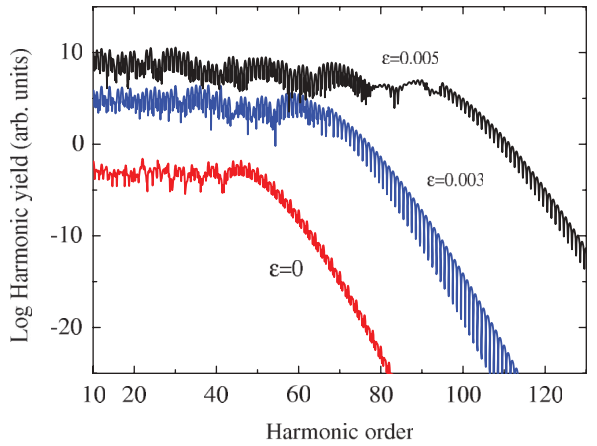

FIG. 15. (Color online) High-order harmonic spectra for hydrogen atoms ($I_p = 0.5$ a.u.) and interacting with a monochromatic field of frequency $\omega = 0.057$ a.u. and intensity $I = 3 \times 10^{14}$ W/cm^2. Red, blue, and black colors depict the cases with $\epsilon = 0$, $\epsilon = 0.003$, and $\epsilon = 0.005$, respectively. All the HHG spectra are scaled for clarity.

Furthermore, it seems that both odd and even harmonics are present in the total spectra. At the lower regime of the spectra, one set of harmonics is a bit more dominant than the others while at a higher regime both odd and even harmonics have the same weight.

In Fig. 15 we compute the HHG spectra for homogeneous fields (red colored spectra) and nonhomogeneous fields with $\epsilon = 0.003$ (blue colored spectra) and $\epsilon = 0.005$ (black colored spectra), respectively. For all three cases, the HHG cutoff is in good agreement with the trajectories analysis represented in the previous section and with the full three-dimensional (3D) numerical calculations of Ref. [21]. For the case with $\epsilon = 0$, the cutoff is at around harmonic 45ω and for $\epsilon = 0.003$ the cutoff is at around harmonic 73ω. The field with $\epsilon = 0.005$ leads to the largest cutoff at around harmonic 93ω. For the latter case, there is less interference in the region corresponding to the harmonics 90ω to 100ω. This behavior is expected since there are just two trajectories which contribute to such cutoff as shown in Fig. 10.

IV. CONCLUSION

In this work, we show how the quantum orbits manifest themselves in spatially inhomogeneous fields. We show that in nonhomogeneous fields, the electron tunnels with two different canonical momenta: One leads to a higher cutoff and the other to a lower one. Furthermore, we demonstrate that for an electron tunneling at the field maxima the tunneling time becomes larger when it recombines at a later time, while for the electron tunneling at the field minima the tunnel time becomes smaller as it recombines at the later time. In fact, as we go from the shorter pairs to the longer ones, the trajectories from the minimum and maximum of the cycle moves toward each other until they collapse on each other at the field crossing. The nonhomogeneity character of the field determines this collapse. For larger nonhomogeneity strength the electron only returns to the core if it follows the shortest pair of trajectories. In addition, for some of the trajectories we can not define the conventional pair of long and short orbits. The former orbit corresponds to the case when the electron leaves a bit earlier and returns a bit later and the latter case gives the trajectories in which an electron leaves a bit later and returns a bit earlier to the ionic core. Indeed, in here, if the electron leaves earlier it will then return earlier and if it leaves later then it will return later. We also demonstrate that in the case of linear nonhomogeneous fields both odd and even harmonics are present in the HHG spectra. At the lower harmonics one is a bit more dominant than the others while at higher harmonic order they both have equal weight. Within our model, we show that the HHG cutoff extends to the larger harmonics as a function of the inhomogeneity strength.

ACKNOWLEDGMENTS

We acknowledge the financial support of the MINCIN project FIS2008-00784 TOQATA (M. F. C. and M.L.); ERC Advanced Grant QUAGATUA, Alexander von Humboldt Foundation and Hamburg Theory Prize (M. L.). We thank Samuel Markson for useful comments and suggestions.

[1] A. McPherson, G. Gibson, H. Jara, U. Johann, T. S. Luk, I. A. McIntyre, K. Boyer, and C. K. Rhodes, J. Opt. Soc. Am. B **4**, 595 (1987).

[2] A. L'Huillier, K. J. Schafer, and K. C. Kulander, J. Phys. B **24**, 3315 (1991).

[3] F. Krausz and M. Ivanov, Rev. Mod. Phys. **81**, 163 (2009).

[4] R. Kienberger, E. Goulielmakis, M. Uiberacker, A. Baltuska, V. Yakovlev, F. Bammer, A. Scrinzi, T. Westerwalbesloh, U. Kleineberg, U. Heinzmann *et al*., Nature (London) **427**, 817 (2004).

[5] M. Drescher, M. Hentschel, R. Kienberger, M. Uiberacker, V. Yakovlev, A. Scrinzi, T. Westerwalbesloh, U. Kleineberg, U. Heinzmann, and F. Krausz, Nature (London) **419**, 803 (2002).

[6] P. B. Corkum, Phys. Rev. Lett. **71**, 1994 (1993).

[7] H. Niikura, D. M. Villeneuve, and P. B. Corkum, Phys. Rev. Lett. **94**, 083003 (2005).

[8] J. Itatani, J. Levesque, D. Zeidler, H. Niikura, H. Pepin, J. C. Kieffer, P. B. Corkum, and D. M. Villeneuve, Nature (London) **432**, 867 (2004).

[9] J. Tate, T. Auguste, H. G. Muller, P. Salières, P. Agostini, and L. F. DiMauro, Phys. Rev. Lett. **98**, 013901 (2007).

[10] P. Colosimo, G. Doumy, C. I. Blaga, J. Wheeler, C. Hauri, F. Catoire, J. Tate, R. Chirla, A. M. March, G. G. Paulus *et al*., Nat. Phys. **4**, 386 (2008).

[11] S. Kim, J. Jin, Y.-J. Kim, I.-Y. Park, Y. Kim, and S.-W. Kim, Nature (London) **453**, 757 (2008).

[12] P. Mühlschlegel, H.-J. Eisler, O. J. F. Martin, B. Hecht, and D. W. Pohl, Science **308**, 1607 (2005).

[13] P. J. Schuck, D. P. Fromm, A. Sundaramurthy, G. S.Kino, and W. E. Moerner, Phys. Rev. Lett. **94**, 017402 (2005).

[14] M. F. Ciappina, J. Biegert, R. Quidant, and M. Lewenstein, Phys. Rev. A **85**, 033828 (2012).

[15] M. Protopapas, C. H. Keitel, and P. L. Knight, Rep. Prog. Phys. **60**, 389 (1997).

[16] T. Brabec and F. Krausz, Rev. Mod. Phys. **72**, 545 (2000).

[17] P. Sailères, A. L'Huillier, P. Antoine, and M. Lewenstein, *Study of Spatial and Temporal Coherence of High Order Harmonics, in Advances of Atomic and Molecular Physics,* edited by B. Bederson and H. Walther (Academic Press, New York, 1999).

[18] A. L'Huillier and M. Lewenstein, *Principles of Single Atom Physics: High-Order Harmonic Generation, Above-Threshold Ionization and Non-Sequential Ionization, in Strong Field Laser Physics, Springer Series in Optical Sciences*, edited by T. Brabec (Springer, Berlin, 2008).

[19] I.-Y. Park, S. Kim, J. Choi, D.-H. L. Y.-J. Kim, M. F. Kling, M. I. Stockman, and S.-W. Kim, Nat. Phot. **5**, 677 (2011).

[20] A. Husakou, S.-J. Im, and J. Herrmann, Phys. Rev. A **83**, 043839 (2011).

[21] I. Yavuz, E. A. Bleda, Z. Altun, and T. Topcu, Phys. Rev. A **85**, 013416 (2012).

[22] M. F. Ciappina, S. S. Aćimović, T. Shaaran, J. Biegert, R. Quidant, and M. Lewenstein, arXiv:1204.5911v1.

[23] M. Sivis, M. Duwe, B. Abel, and C. Ropers, Nature (London) **485**, 1(E) (2012).

[24] S. Kim, J. Jin, Y.-J. Kim, I.-Y. Park, Y. Kim, and S.-W. Kim, Nature (London) **485**, 2(E) (2012).

[25] P. B. Corkum (private communication).

[26] W. Gordon, Z. Phys. **40**, 117 (1926).

[27] D. M. Volkov, Z. Phys. **94**, 250 (1935).

[28] M. Lewenstein, P. Balcou, M. Y. Ivanov, A. L'Huillier, and P. B. Corkum, Phys. Rev. A **49**, 2117 (1994).

[29] W. Becker, A. Lohr, M. Kleber, and M. Lewenstein, Phys. Rev. A **56**, 645 (1997).

[30] F. Süßmann and M. F. Kling, Proc. SPIE **8096**, 80961C (2011).

[31] C. H. Edwards and D. E. Penney, *Differential Equations Computing and Modeling*, 4 ed. (Prentice Hall, New York, 2007).

[32] N. Bleinstein and R. A. Handelsman, *Asymptotic Expansion on Integrals* (Dover, New York, 1986).

[33] P. Salières, B. Carré, L. L. Déroff, F. Grasbon, G. Paulus, H. Walther, R. Kopold, W. Becker, D. B. Milošević, A. Sanpera *et al*., Science **292**, 902 (2001).

[34] C. Figueira de Morrison Faria, H. Schomerus, and W. Becker, Phys. Rev. A **66**, 043413 (2002).